Dalton Transactions

ROYAL SOCIETY OF CHEMISTRY

PAPER

View Article Online
View Journal | View Issue

Cite this: *Dalton Trans.*, 2026, **55**, 4128

Analysis of the charge/discharge mechanism of an Fe-containing Li_2S positive electrode material and its visualization by computational simulation

Tomonari Takeuchi, [a] Yoyo Hinuma, *[a] Koji Ohara,†[b] Hiroyuki Kageyama,[c] Koji Nakanishi,‡[c,d] Toshiaki Ohta,[d] So Fujinami, [b,c] Hisao Kiuchi §[c] and Hikari Sakaebe¶[a]

The structure and charge/discharge mechanism of an Fe-containing Li_2S-based positive electrode material (Li_8FeS_5) were investigated using X-ray scattering and absorption spectroscopy analyses. Conventional XRD measurements indicated that Li_8FeS_5 adopts a low-crystalline Li_2S structure (antifluorite; space group $Fm\bar{3}m$), and pair distribution function (PDF) analyses suggested that Fe ions occupy the vacant cation sites. Structural rearrangement occurred during the first charge, resulting in the formation of an inhomogeneous local structure around S atoms. The structural change was irreversible when charged to 3.0 V but not at 2.6 V *vs.* Li^+/Li, which may be the reason for the low discharge capacity in a normal electrochemical test. Significant disproportionation of S–S distances (*ca.* 4.0 Å, corresponding to the nearest-neighbor S–S distance in the antifluorite structure) was observed when charged to 3.0 V, and such irreversible disproportionation was observed mainly around the S–S pairs away from the Fe atoms. The atomic rearrangements during charge/discharge processes were also modeled using neural network potential calculations, which were reasonably consistent with the PDF results.

Received 8th December 2025,
Accepted 5th February 2026

DOI: 10.1039/d5dt02938d

rsc.li/dalton

1. Introduction

The demand for high-energy storage systems is increasing because of their applications in electric vehicles and electric power grid systems. Next-generation batteries are required that have much higher energy density than the *ca.* 200 Wh kg^{-1} of conventional lithium-ion batteries.[1,2] Among them, lithium–sulfur (Li–S) batteries are promising because of their theoretically high energy density of up to *ca.* 2600 Wh kg^{-1} in a closed system that does not involve gaseous components.[3]

Lithium sulfide (Li_2S) is a potential positive electrode active material for Li–S batteries with a high theoretical capacity (*ca.* 1170 mAh g^{-1}). An advantage is that a variety of negative electrode materials without lithium sources, such as graphite and silicon, can be used in a practical battery system.[4–10] However, Li_2S is electrically resistive (<10^{-10} S cm^{-1}), giving rise to low practically observed capacity values in cells. Several attempts have been made to enhance the conductivity of Li_2S, such as forming composites with carbon (Li_2S–C)[7,9,10] or metals (Li_2S–Fe, Li_2S–Cu, and Li_2S–V).[4–6,11] Our material design concept features the Fe-containing polysulfide material Li_xFeS_y, with a conductivity of the order of 10^{-5} S cm^{-1}.[8,12] This Li_xFeS_y consists of an Fe-substituted low-crystalline Li_2S and shows characteristic electrochemical performance in cells with nonaqueous liquid electrolytes. A typical Li_8FeS_5 cell has a discharge capacity of *ca.* 330 mAh g^{-1} after charging to 3.0 V, and it increases to *ca.* 810 mAh g^{-1} when the charge voltage is restricted to 2.6 V.[8,13] Several analyses using ^{7}Li NMR and XPS measurements revealed that charge compensation was mainly accomplished by S, accompanied by breakage and formation of S–S polysulfide bonds that alter the local atomic configuration to amorphous upon Li extraction and then to the antifluorite structure after Li insertion. The present Li extraction/insertion mechanism is neither a topotactic nor a conversion-type

[a]*National Institute of Advanced Industrial Science and Technology (AIST), Midorigaoka 1-8-31, Ikeda, Osaka 563-8577, Japan. E-mail: y.hinuma@aist.go.jp*
[b]*The Research & Utilization Division, Japan Synchrotron Radiation Research Institute (JASRI), 1-1-1 Kouto, Sayo, Hyogo 679-5198, Japan*
[c]*Office of Society-Academia Collaboration for Innovation, Kyoto University, Uji, Kyoto 611-0011, Japan*
[d]*Synchrotron Radiation Center, Ritsumeikan University, 1-1-1 Noji-Higashi, Kusatsu, Shiga 525-8577, Japan*
†Present address: Shimane University, 1060 Nishikawatsu-cho, Matsue, Shimane 690-8504, Japan.
‡Present address: University of Hyogo, 3-1-2 Koto, Kamigori-cho, Ako-gun, Hyogo 678-1205, Japan.
§Present address: Research Center for Energy and Environmental Materials (GREEN), National Institute for Materials Science (NIMS), Tsukuba, Ibaraki 305-0044, Japan.
¶Present address: Kyushu University, 6-1 Kasugakoen, Kasuga, Fukuoka 816-8580, Japan.

reaction.[14] Although the electrochemical charge/discharge mechanism is revealed to some extent, detailed structural changes of Li_8FeS_5 remain unclear, particularly those depending on the charge voltage, which are significant for understanding the difference in the subsequent discharge capacity. Clarifying this mechanism is necessary for designing Li_xFeS_y-based polysulfide materials as well as for assembling Li_xFeS_y-based practical battery systems with further improved electrochemical performance.

In the present work, we have analyzed structural changes in Li_8FeS_5 during Li extraction/insertion reactions, depending on the charge voltage, using X-ray scattering and absorption spectroscopy. These techniques are advantageous for analyzing the local structure of, particularly, amorphous and/or low-crystalline materials. We also computationally derived reasonable crystal structure models of Li_xFeS_5 using neural network potential (NNP) calculations and verified the models with experimental results.

2. Experimental methods

Li_8FeS_5 samples were prepared as reported previously:[8] blended powder of Li_2S and FeS in a 4 : 1 molar ratio was treated by spark plasma sintering (SPS; SPS-3.20 MK-IV, Fuji Electronic Industrial, Japan) at 600 °C for 3 min under an argon atmosphere. The product was blended with acetylene black (AB) powder at a 9 : 1 weight ratio and then mechanically milled for 8 h using a pulverizer (Model No. MC-4A, Ito Seisakusho, Japan) at a rotation speed of 1000 rpm to yield Li_8FeS_5 samples. Since Li_2S and Li_8FeS_5 are very sensitive to atmospheric moisture, all procedures except the SPS and mechanical milling were carried out in an argon-filled glove box; the SPS and mechanical milling were performed under atmospheric conditions using the argon-filled container and pot wherein Li_2S and Li_8FeS_5 were enclosed.

The phase purity of the sample was checked by X-ray diffraction (XRD) measurements (RINT TTR-III, Rigaku, Japan) using monochromatic Cu K_α radiation within the 2θ range of 10°–125°. Each sample was covered with Kapton film in an argon-filled glove box before measurement, and the measurement was carried out within 1 h to suppress reactions with atmospheric moisture. The atomic structure of each sample was examined by high-energy X-ray total scattering measurements carried out at beamline BL28XU at SPring-8.[15] The incident X-ray energy was 38.0 keV, and scattering patterns measured with a Q-range from 0.3 to 17 $Å^{-1}$ were analyzed using the reduced pair distribution function (RPDF), $G(r)$, where r is the distance.[16–19] The RPDF is defined as

$$G(r) = \frac{2}{\pi}\int_{Q_{min}}^{Q_{max}} Q\{S(Q) - 1\}\sin(Q_r)\mathrm{d}Q, \quad (1)$$

where Q_{min} and Q_{max} are the lower and upper limits of the measured Q and $S(Q)$ is the structure factor. A vacuum chamber was used to suppress air scattering around the sample. The measured datasets were corrected for absorption, background, and polarization effects, followed by normalization to obtain the RPDF, according to a procedure detailed elsewhere.[17] The valence state and local structure of S atoms for the sample electrodes were examined by S K-edge X-ray absorption fine structure (XAFS) spectroscopy, which was carried out at the soft X-ray double crystal monochromator beamline BL-10 in the Synchrotron Radiation Center, Ritsumeikan University.[20] The incident X-ray beam was monochromatized with a Ge(111) crystal ($2d$ = 6.532 Å) pair, and the photon energy was calibrated with the strong resonance of K_2SO_4 (S $1s \rightarrow t_2$) appearing at 2481.7 eV.[21] All the samples were transferred from an argon-filled glove box to a XAFS chamber using a vessel without exposure to air. Spectra were taken with the total electron yield (TEY) mode.[20] We also carried out Fe K-edge XAFS measurements with the transmission mode using an X-ray spectrometer (EXAC-820, Technos). The X-ray generator with a Mo rotating anode and a LaB_6 cathode was operated at a voltage of 20 kV and a current

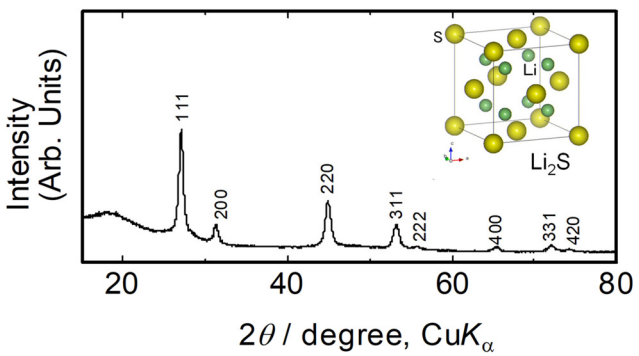

Fig. 1 XRD pattern (using Cu K_α radiation) of Li_8FeS_5 and its crystal structure.

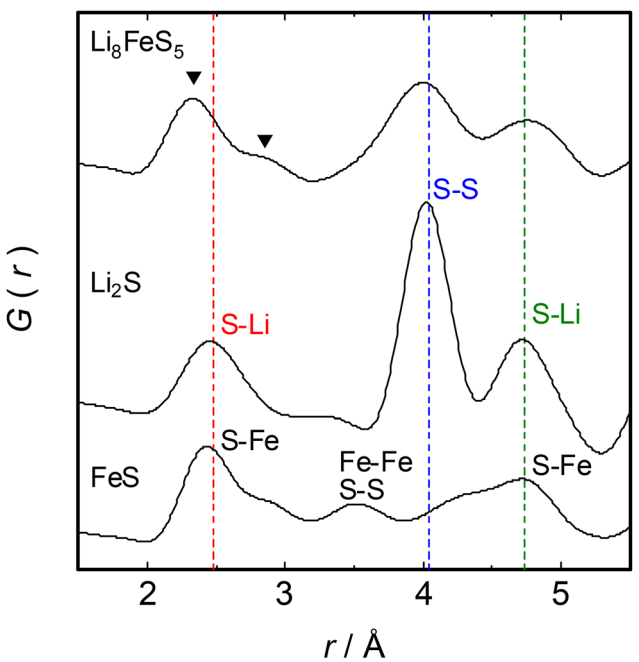

Fig. 2 X-ray RPDF data of Li_8FeS_5. Data for Li_2S and FeS are also shown for comparison.

of 200 mA. The incident X-ray beam was monochromatized with a Ge(400) Johansson curved crystal ($2d$ = 2.828 Å).

Electrochemical lithium extraction/insertion reactions were carried out using lithium coin-type cells. The working electrode consisted of a mixture of 11.1 mg Li_8FeS_5 sample (containing 10% (1.1 mg) AB), 3.9 mg additional AB powder, and 0.5 mg Teflon powder pressed into a 15 mm diameter tablet under a pressure of 10 MPa. The electrochemical test cell was constructed in a stainless steel coin-type configuration. The negative electrode was a 15 mm diameter and 0.2 mm thick disk of Li foil, and the separator was a microporous polyolefin sheet. The solution of 1 M $LiPF_6$ in a 50 : 50 mixture of ethylene carbonate (EC) and dimethyl carbonate (DMC) by volume (Kishida Chemical, battery grade) was used as the electrolyte. Each cell was assembled in an argon-filled glove box. Electrochemical measurements were carried out at 30 °C initially with charging after standing overnight on open circuit. A TOSCAT-3100 (Toyo System) was used at a current

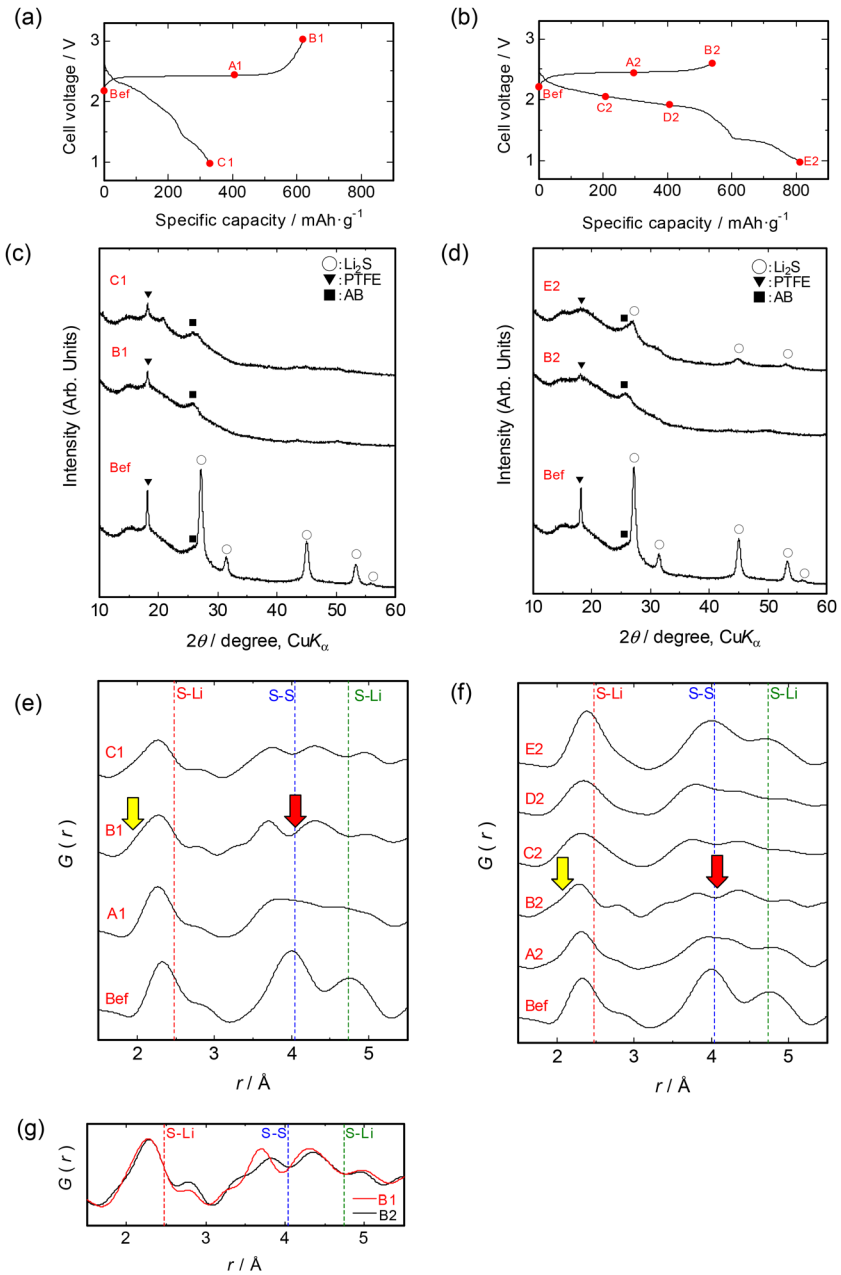

Fig. 3 (a and b) Charge and discharge profiles for the Li_8FeS_5 sample cells at 46.7 mA g^{-1} (corresponding to 0.04C for $2e^-/Li_2S$) with the voltage range of (a) 3.0–1.0 and (b) 2.6–1.0 V *vs.* Li^+/Li. Samples used for analyses are denoted by filled red circles. (c and d) XRD patterns and (e and f) X-ray RPDF data for the Li_8FeS_5 sample during electrochemical cycling with the voltage range of (c), (e) 3.0–1.0 and (d), (f) 2.6–1.0 V *vs.* Li^+/Li. Red and yellow arrows in (e and f) indicate the inhomogeneous S–S distances and short S–S bonds analogous to S_8, respectively. The sample labels, such as Bef and B1, correspond to the positions in the charge and discharge process shown in 3(a) and (b). (g) Comparison of RPDF data for samples B1 and B2. The vertical lines represent the $G(r)$ peak positions of S–Li and S–S in Li_2S.

density of 46.7 mA g^{-1} (corresponding to 0.04C for $2e^-/Li_2S$) between 2.6 (or 3.0) and 1.0 V *vs.* Li^+/Li.

3. Computational methods

3.1. Formation energy calculation

NNP calculations were conducted using the Matlantis package from Preferred Networks with the universal PreFerred Potential (PFP)[22] version 7.0.0. The NNP is trained on the Perdew–Burke–Ernzerhof (PBE) generalized gradient approximation (GGA) to density functional theory (DFT).[23] The PFP is already fully trained by the developers based on calculations using the VASP code[24,25] and is available as a "take it or leave it" potential; the user cannot modify it. Both lattice parameters and internal coordinates were allowed to fully relax unless stated otherwise. Relaxation of Li_xFeS_5 is a non-trivial issue, especially when x is small, where there are many vacancies and significant relaxation happens to both lattice parameters and internal coordinates. A four-step relaxation protocol was adopted using the limited memory Broyden–Fletcher–Goldfarb–Shanno optimizer as implemented in the Matlantis package. The maximum force and maximum displacement of atoms in each iteration were changed from (10 eV $Å^{-1}$, 0.002 Å) to (1, 0.005), (0.03, 0.01), then (0.005, 0.02). The allowed maximum number of iterations in each step was 20 000 steps. The initial maximum force often exceeded 10 eV $Å^{-1}$, hence the displacement should be small at the very start of the optimization and then gradually increased to accelerate convergence while suppressing local minima.

3.2. Model generation

The crystal structure of Li_xFeS_5 was based on the antifluorite structure. Supercells of Li_xFeS_5, or $Li_{8x}Fe_8\square_{72-8x}S_{40}$, were obtained by making a $\sqrt{5} \times \sqrt{5} \times 2$ supercell of the antifluorite conventional cell. Here, $\square$ represents vacancies and $x \leq 9$. The initial lattice parameter was set to a = 5.70257 Å for the conventional cell, which is the NNP optimized value of Li_2S.

Determining how to distribute Li, Fe and vacancies on the cation sublattice is a subtle problem. 200 Li/Fe/vacancy configurations of Li_8FeS_5 were randomly generated, and the lowest energy configuration was used as the base model.

The distribution of Fe was fixed to this base model, and Li-deficient models were obtained by removing Li from this Li_8FeS_5 base model as follows. Not all Li sites are equivalent, and Li could be more easily extracted from some sites than others. This study categorized Li sites based on the nearest neighbor cations around a Li site. There are six nearest neighbor cation sites for each cation site; note that the cation sublattice is a simple cubic lattice. A valence score was defined, where a nearest neighbor (NN) vacancy, Li, and Fe contribute 0, 1, and 2 to the score, respectively. The score reflects the nominal valences of $Li^+{}_8Fe^{2+}S^{2-}{}_5$. The valence score of each Li site is 6 in a defect-free antifluorite structure Li_2S. Extraction multipliers m_-, m_6, and m_+ were defined for Li sites with valence scores less than 6, equal to 6, and greater than 6,

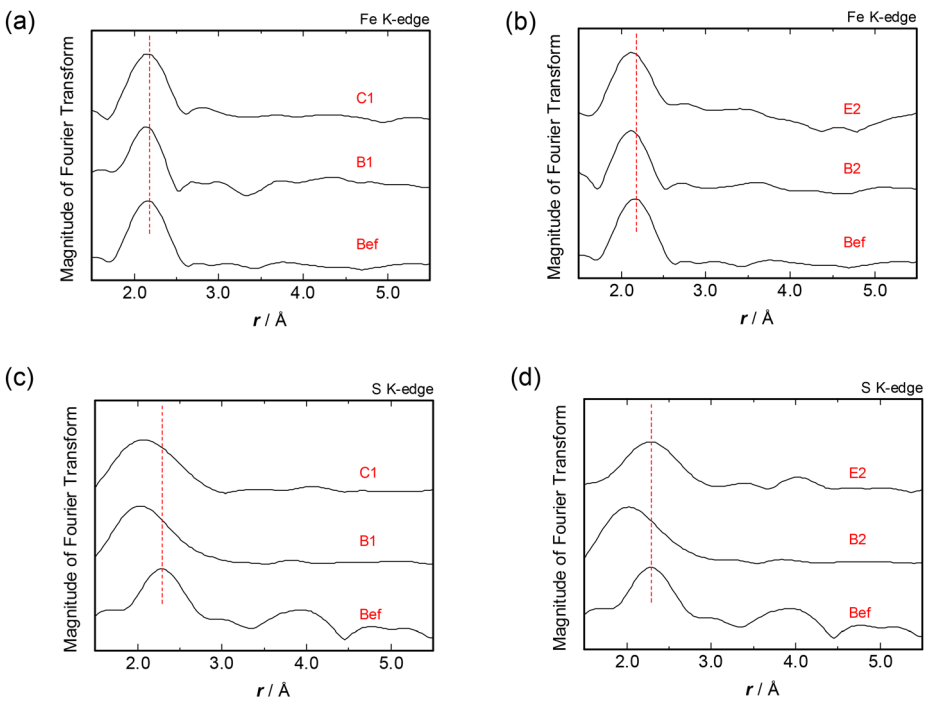

Fig. 4 The k^3-weighted EXAFS Fourier transform magnitude for the Li_8FeS_5 positive electrodes before the electrochemical tests and after the 1st charge and discharge process with the voltage range of (a), (c) 3.0–1.0 V and (b), (d) 2.6–1.0 V *vs.* Li^+/Li. EXAFS data were based on (a), (b) Fe K-edge and (c), (d) S K-edge spectra. The sample labels, such as Bef and B1, correspond to positions in the charge and discharge process shown in Fig. 3(a) and (b). Phase shifts are corrected in all the figures.

respectively. The removal probability of a Li was set to be proportional to its extraction multiplier.

Three types of multiplier combinations were examined in this work, namely (m_-, m_6, and m_+) = (1, 2, 3), (1, 1, 1), and (3, 2, 1), respectively, which are hereafter denoted as 123, 111, and 321 extractions, respectively. 123 and 321 extractions preferentially remove Li surrounded by high and low-valence cations, respectively, while all Li are removed with equal probability for the 111 extraction. 50 kinds of Li/vacancy removal patterns for each of the 123, 111, and 321 extraction methods were randomly generated. The lowest energy model among these three extraction types was used for analysis at each Li concentration. Models with lattice parameters fixed to Li_8FeS_5 were additionally evaluated for Li_3FeS_5, and the lowest energy model is denoted as "Li_3FeS_5 Fix".

The Li-excess Li_9FeS_5 model was obtained from the Li_8FeS_5 base model by simply replacing cation sublattice vacancies with Li. There is only one such model. $Li_{10}FeS_5$ models were derived from the Li_9FeS_5 model as follows. The antifluorite structure can be regarded as a superimposition of two simple cubic sublattices forming the rocksalt structure, where only half of the anion sublattice is occupied in an ordered manner. Li_9FeS_5 may be expressed as $(Li_9Fe)(\square_5S_5)$, and $Li_{10}FeS_5$ is viewed as $(Li_9Fe)(Li\square_4S_5)$. The brackets represent the stoichiometries of the cation and anion sites, respectively. The nearest neighbors (NNs) of Li in the anion sublattice are eight cations in the cation sublattice, and the next NNs are six S. 150 random Li/vacancy distributions in the non-S atom sites in the cubic anion sublattice were considered, where Li was never inserted in an anion sublattice vacancy next to a Fe atom. The lowest energy model was considered for $Li_{10}FeS_5$.

3.3. Computational PDF derivation

Computationally, the PDF, $g(r)$, can be expressed as a superimposition of delta functions, but such a PDF is difficult to visualize and compare with experimental data. The delta functions were broadened with a Gaussian with parameter σ, and the (non-normalized) PDF is defined in this study as a function of distance r, as follows,

$$g(r) = \sum_{ij} \frac{1}{4\pi {r_{ij}}^2} \left(\frac{1}{2\pi\sigma}\right) \exp\left(-\frac{(r-r_{ij})^2}{2\sigma^2}\right), \quad (2)$$

where r_{ij} is the distance between atoms i and j. The summation may be over all element combinations or limited to a certain pair, such as S–Li only. The atom i is within a supercell, while the other atom j may be outside the supercell. PDFs were calculated within an arbitrary cutoff distance. The broadening reflects the thermal fluctuation near an equilibrium position at a finite temperature.

An element-weighed PDF, $g'(r)$, is defined as

$$g'(r) = c \sum_{ij} \frac{Z_i Z_j}{{r_{ij}}^2} \exp\left(-\frac{(r-r_{ij})^2}{2\sigma^2}\right) \quad (3)$$

Here, c is an arbitrary scaling constant. The shape of the PDF is important, especially the peak positions, but usually the absolute value is not. The contribution of a bond to the total PDF is weighed by the product of Z_i and Z_j, which are the atomic numbers of atoms i and j, respectively. The atomic form factor is approximately proportional to the atomic number, and $S(Q)$ is proportional to the atomic form factors of the two atoms constituting a bond.

The PDFs $g(r)$ and $g'(r)$ were calculated at binsize b intervals. Denoting the maximum considered value as r_{max}, the PDF from $r = 0$ to r_{max} was returned as an array with size r_{max}/b. The exponential term for bond i–j was evaluated for r between $r_{ij} - 4\sigma < r < r_{ij} + 4\sigma$ to reduce computational cost; note that $\exp(-(4\sigma)^2/2\sigma^2)$ is as small as 0.0003. The RPDF and PDF are related by

$$G(r) = 4\pi r \rho_0 \{g(r) - 1\}, \quad (4)$$

where ρ_0 is the atom density. However, conversion from $g'(r)$ and $G(r)$ is not trivial and is not attempted. Peaks of $g'(r)$ and $G(r)$ appear at almost the same positions, so conversion is not necessary for peak position comparison.

3.4. Density of states calculation

The electronic density of states (DOS) of Li_2S and the lowest energy Li_8FeS_5 model were calculated using the VASP program.

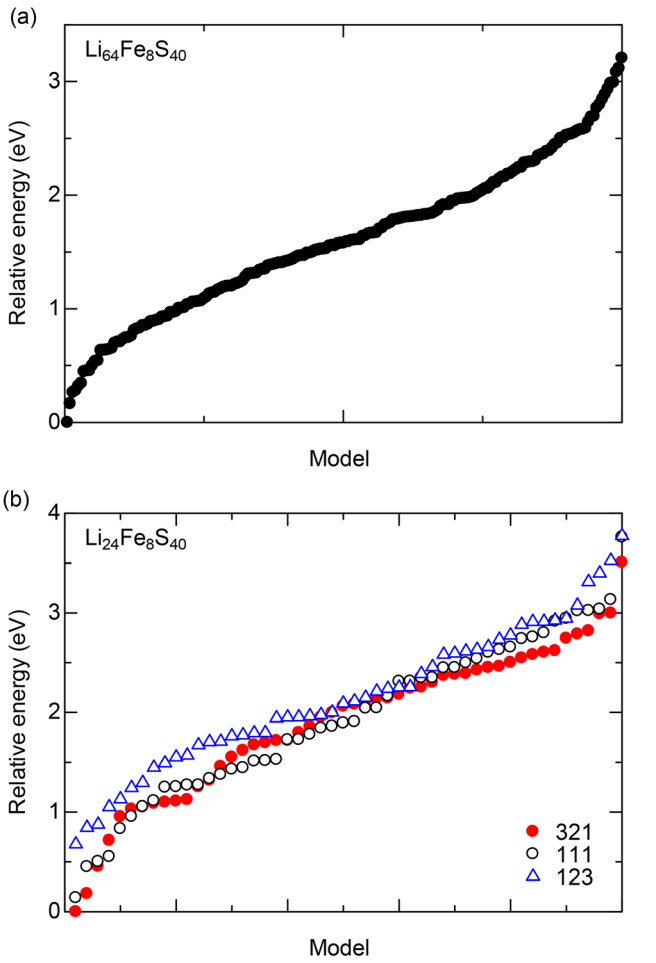

Fig. 5 Relative energies, in ascending order, of (a) 200 $Li_{64}Fe_8S_{40}$ models and (b) 50 $Li_{24}Fe_8S_{40}$ models each for the 123, 111, and 321 Li extraction strategies

The lattice parameters were fixed to NNP calculations. The internal coordinates were relaxed using the PBEsol functional,[26] a modification of the PBE functional tuned for solids, and the DOS was obtained using PBEsol.

4. Results and discussion

4.1. Experimental findings

The Li_8FeS_5 powder was greyish black in appearance, and its XRD pattern is shown in Fig. 1. All peaks are rather broad and indexed by the cubic unit cell (space group $Fm\bar{3}m$), and the estimated lattice parameter (a = 5.7020(8) Å) is smaller than that of the pristine Li_2S (a = 5.7158(1) Å). This is due to the partial substitution of Fe^{2+} (0.66 Å) for Li^+ (0.74 Å), and therefore the Li_8FeS_5 sample has a Fe-substituted low-crystalline Li_2S structure (antifluorite).[8] This is a metastable phase because it decomposes to mainly crystalline Li_2S and Li_2FeS_2 after re-treatment by SPS at 600 °C. Fig. 2 shows the experimentally obtained RPDF, $G(r)$, where the S–S and S–Li peaks of Li_2S at *ca.* 4.0 and 4.7 Å, respectively, are also observed as the peak positions of Li_8FeS_5. The single S–Li peak in Li_2S at *ca.* 2.5 Å becomes a double peak in Li_8FeS_5, as indicated using down-pointing triangles. The larger peak at shorter distance (r)

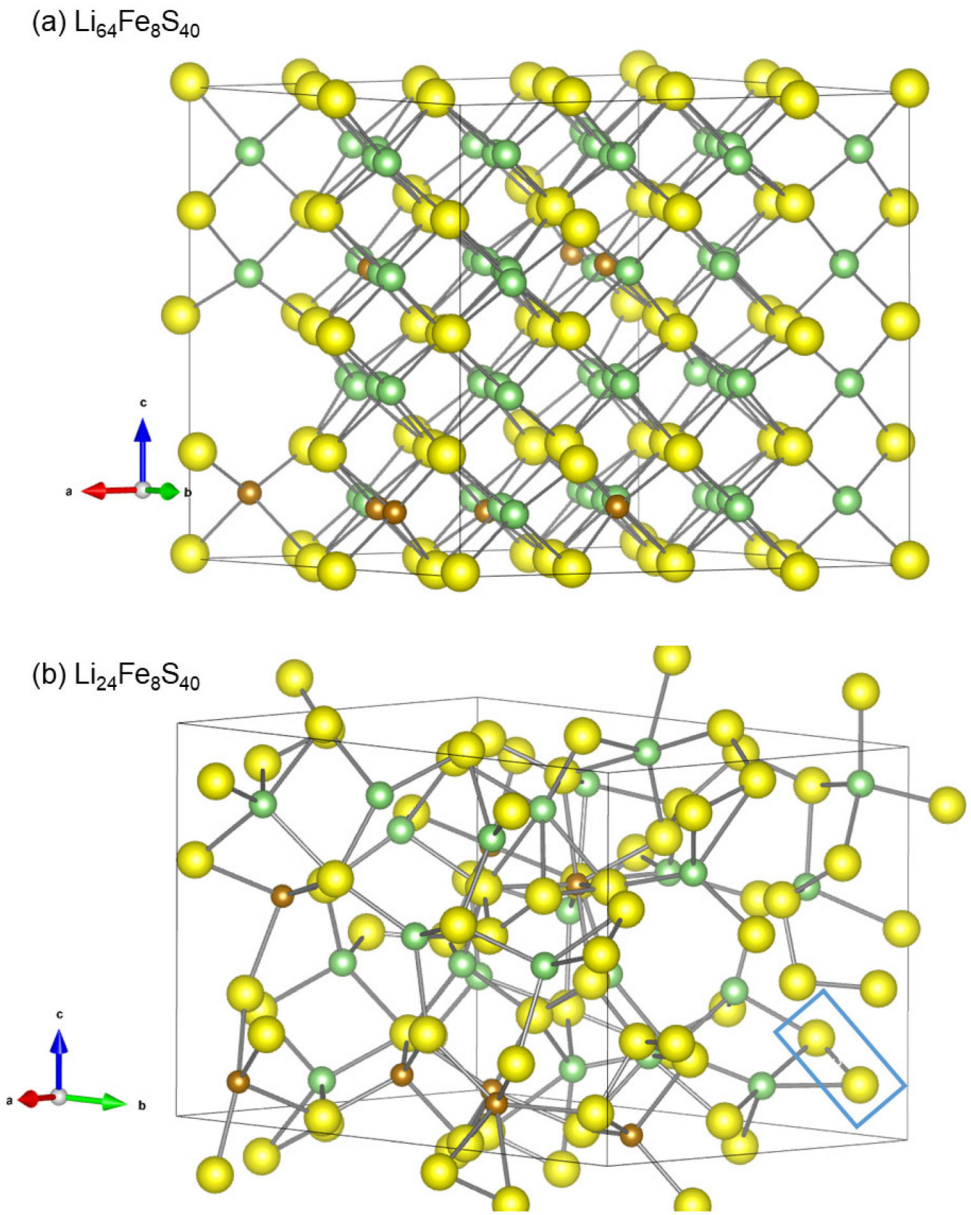

Fig. 6 The lowest energy model among the (a) 200 randomly constructed models of $Li_{64}Fe_8S_{40}$ and (b) the 150 considered models of $Li_{24}Fe_8S_{40}$. Green, brown, and yellow balls correspond to Li, Fe, and S, respectively. S–S bonds with distances less than 2.2 Å are shown, and one example is shown in the blue box.

is the S–cation nearest neighbor (NN) peak, while the smaller peak at larger r is assigned to the cation–cation NN peak, as discussed later. The cation–cation peaks are not found in the RPDF of Li_2S because of the low atomic scattering factor of Li.

Fig. 3(a and b) show the characteristic charge/discharge profiles of the Li_8FeS_5 cell with charge voltages of 3.0 and 2.6 V *vs.* Li^+/Li, respectively. The charge capacity showed rather similar values irrespective of the upper voltage (621 and 543 mAh g^{-1}, respectively). The discharge capacity was *ca.* 330 mAh g^{-1} after charging to 3.0 V, while it increased to *ca.* 810 mAh g^{-1} when the charge voltage was restricted to 2.6 V. During the initial charge/discharge cycling, the apparent composition of the active material can be estimated from the measured capacity values, as $Li_8FeS_5 \rightarrow Li_{1.7}FeS_5 \rightarrow Li_{5.0}FeS_5$ and $Li_8FeS_5 \rightarrow Li_{2.5}FeS_5 \rightarrow Li_{10.7}FeS_5$ for charging to 3.0 V and 2.6 V, respectively. Cycle performances of the present Li_8FeS_5 cells, depending on the charge voltage, are shown in Fig. S1(a) in SI, where data for the cells starting with discharging are additionally shown for reference; Li insertion to Li_8FeS_5 seems to deteriorate long-term structural reversibility. Although the present electrochemical tests were carried out using a Li metal negative electrode to focus on the analyses of Li extraction/insertion mechanism on Li_8FeS_5, we observed normal electrochemical cycling in Si/Li_8FeS_5 cells, confirming an advantage in practical battery systems without a Li-containing negative electrode as described in the Introduction, which will be reported subsequently elsewhere.

To clarify the charge/discharge mechanism depending on the charge voltage, we disassembled the Li/Li_8FeS_5 cells during the charge/discharge process at several steps, denoted as red circles in Fig. 3(a and b), and carried out *ex situ* XRD measurements. As shown in Fig. 3(c), the antifluorite structure peaks, which coincide with the peaks of Li_2S, disappeared after charging to 3.0 V *vs.* Li^+/Li (B1) and did not reappear after discharge (C1). In contrast, the antifluorite peaks disappeared after charging to 2.6 V *vs.* Li^+/Li (B2) (Fig. 3(d)) but reappeared as broad peaks after discharging (E2). Such a difference was also observed for the cycled samples (Fig. S1(b)). Restricting the charging voltage to 2.6 V thus resulted in a reasonable recovery of the antifluorite structure after Li re-insertion; in fact, the estimated lattice parameter of the E2 sample (a = 5.699(4) Å) was close to that of the Bef sample (a = 5.7020(8) Å).

To examine the local structure of the Li_8FeS_5 sample in detail, we carried out RPDF ($G(r)$) analysis of the high-energy X-ray total scattering data, which is particularly useful for determining the structure of amorphous or low-crystalline samples.[16–19] Some raw data and those after subtracting the background and the contributions from AB and PTFE are shown in Fig. S2 for reference. As shown in Fig. 3(e), charging to 3.0 V (B1) resulted in the disproportionation of S–S distances around 4.0 Å (red arrow) and formation of S–S bonds near 2 Å (slight increase of the RPDF near the yellow arrow), analogous to S_8. These changes remained after discharge (C1), clearly indicating that the $Fm\bar{3}m$ structure was not recovered. On the other hand, as plotted in Fig. 3(f), charging to 2.6 V (B2) caused similar disproportionation of S–S distances around 4 Å and formation of S–S bonds near 2 Å, but the profile after discharge (E2) was close to that before charge. It is noteworthy that the structure partly reverted to the antifluorite structure after charge/discharge cycling within 2.6–1.0 V. Such structural revert was accompanied with the reduction of crystallite size, as was evident from the peak width in XRD (Fig. 3(d)); the estimated crystallite sizes using the peak width at 2θ = 27° were 15 and 6.3 nm for Bef and E2 samples, respectively. The difference in the structure after charge and distance was more evident in the long-range atomic distri-

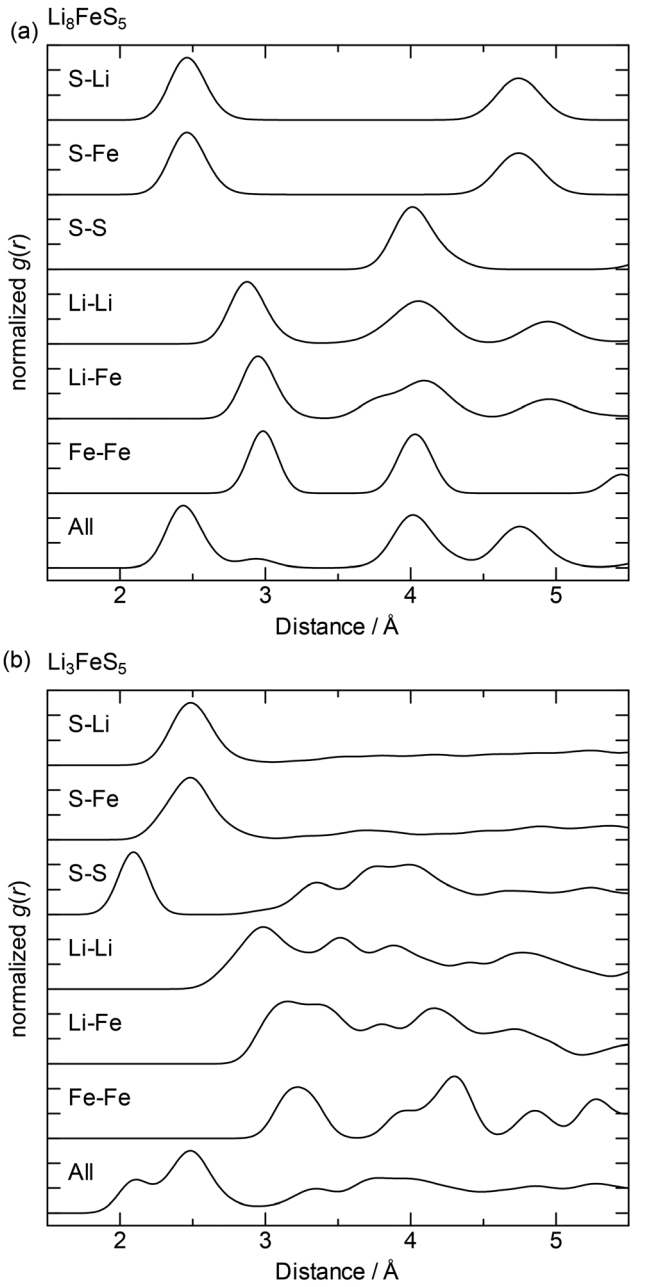

Fig. 7 Calculated PDFs of the lowest energy model for (a) $Li_{64}Fe_8S_{40}$ and (b) $Li_{24}Fe_8S_{40}$.

bution (>*ca.* 10 Å, shown in Fig. S3 in SI). There was no long-range ordering after charging to 3.0 V (B1) and the subsequent Li re-insertion (C1), as indicated by the flat feature of $G(r)$ at >*ca.* 10 Å (Fig. S3(a)). In contrast, long-range ordering was rather recovered after Li re-insertion (E2) when the charging voltage was 2.6 V because the profile is not flat at >*ca.* 10 Å in E2 (Fig. S3(b)). Considering $G(r)$ at short r, Fig. 3(g) compares the profiles at 3.0 V (B1) and 2.6 V (B2), respectively. The profiles near the antifluorite S–cation distance at *ca*. 4.7 Å were almost the same, while those near the antifluorite S–S distance at *ca*. 4.0 V were clearly different; peak separation was more significant in sample B1. More extended disproportionation of S–S distances upon charging to 3.0 V could inhibit recovery of the antifluorite structure during discharge.

The k^3-weighted EXAFS Fourier transform magnitude is shown in Fig. 4, where the EXAFS data were based on (a)(b) Fe K-edge and (c)(d) S K-edge spectra. The charged (B1, B2) and discharged (C1, E2) Fe K-edge curves have very small charge voltage dependence (3.0 and 2.6 V *vs.* Li^+/Li in Fig. 4(a and b), respectively). In contrast, the S K-edge curve after discharge

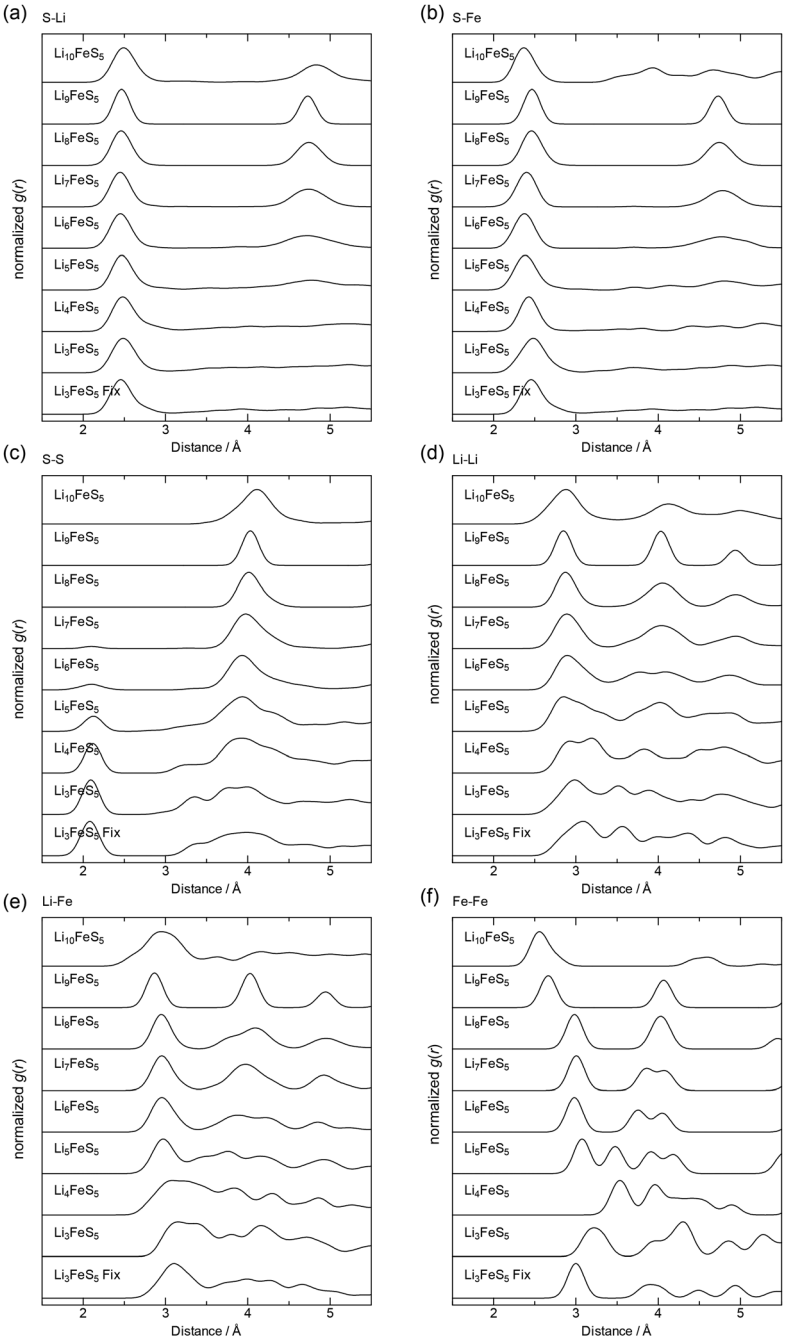

Fig. 8 Calculated PDFs of the lowest energy models for (a) S–Li, (b) S–Fe, (c) S–S, (d) Li–Li, (e) Li–Fe, and (f) Fe–Fe.

(E2) is similar to the initial (Bef) curve when the charge was limited to 2.6 V (Fig. 4(d)), but this is not the case when the charge voltage is 3.0 V (Fig. 4(c)). These results corroborate the insight inferred from the RPDF results in Fig. 3(e and f).

4.2. Computational results

4.2.1 Li_8FeS_5 PDF. Fig. 5(a) shows the formation energies calculated for the 200 Li_8FeS_5 models, sorted by formation energy. A small number of configurations have very low energies, demonstrating the importance of evaluating a large number of models to identify a reasonable configuration when using a brute-force approach based on randomly generated models. Evaluating all possible combinations is unrealistic, even with the removal of identical combinations.[27] The lowest energy configuration adopts the antifluorite structure, as is visualized in Fig. 6(a).

The PDF result, for each pair of species such as S–S and S–Fe, is shown in Fig. 7(a). PDFs are normalized such that the maximum peak has the same intensity. The 2.5 Å S–cation peak, 2.8 Å cation–cation peak, 4.0 Å S–S and cation–cation peaks, and 4.7 Å S–cation peaks are clearly reflected in the "all" PDF, which is the weighted PDF where the contribution from each distance is weighted based on the atomic numbers constituting the pair.

4.2.2. Li_3FeS_5 PDF. Fig. 5(b) shows the formation energies of the evaluated 50 Li_3FeS_5 models for each Li extraction method, sorted by energy for each method. The points for the 123 extraction method are, on the whole, above the other methods in this figure. In other words, the removal of Li near low valence cations is not favored. However, such a trend is not consistently found over various Li concentrations (Fig. S4). Fig. 6(b) shows the lowest energy model. Li_3FeS_5 clearly cannot sustain the antifluorite structure. S–S bonds shorter than 2.2 Å are visualized, and one is shown in the blue box as an example. The PDF of Li_3FeS_5 is shown in Fig. 7(b). The 4.7 Å S–Li and S–Fe peaks in Li_8FeS_5 have completely disappeared in Li_3FeS_5. A new S–S peak appeared at 2.1 Å, while the 4.0 Å S–S peak in Li_8FeS_5 disintegrated, resulting in a very broad feature with small peaks at 3.3, 3.7, and 4.0 Å.

4.2.3. Li_xFeS_5 PDF. Fig. 8 compares the PDFs over all x for each species pair. The lowest energy models, except for the aforementioned $x = 8$ and $x = 3$, are visualized in Fig. S5. In S–Li and S–Fe PDFs (Fig. 8(a and b), respectively), the NN S–Li and S–Fe peak positions are the same regardless of x, which means that S–Li and S–Fe bonds are very rigid. The peak at *ca.* 4.7 Å is sharpest at $x = 9$ and gradually flattens above and below this Li concentration. This peak completely disappears at $x \leq 4$. The S–S peak at *ca.* 4.0 Å is a characteristic peak of the antifluorite structure (Fig. 8(c)). Decreasing the Li content to $x \leq 5$ results in the appearance of a new peak at *ca.* 2.1 Å and substantial broadening of the original peak at *ca.* 4.0 Å. The NN peaks of Li–Li and Li–Fe (Fig. 8(d and e), respectively) stay at the same distance slightly below 3 Å regardless of the Li concentration. The Fe–Fe PDF (Fig. 8(f)) changes significantly with Li concentration, partly because the Fe concentration in the cation site is very low and the number of bonds that contribute to the PDF is very small compared to other element combinations. The *ca.* 4.9 Å peak observed in the Li–Li and Li–Fe PDFs is missing in the Fe–Fe peak because there is no such bond at this distance in the considered models. The *ca.* 3.0 and 4.0 Å peaks come from one and two distances in a supercell, respectively. Changes in the lengths of these distances substantially affect the PDF shape. When $x = 10$, the high cation concentration in the supercell forces significant relaxation of Fe positions from the high symmetry positions of the fluorite structure, resulting in a short Fe–Fe distance peak.

4.2.4. Deformation in Li_xFeS_5. The shear deformation with relaxation was evaluated using a shear index $s = abc/V$, where a, b, and c are the lattice parameters of the supercell, and V is the volume. This s has the minimum value of 1 when the supercell is orthogonal, and increases as the shear deformation increases. Fig. S6 shows s for the lowest energy model *versus* x. The s is almost 1 for $x \geq 6$ and rapidly increases when x is reduced in the range $x \leq 5$. Fig. 6(b) and 8, and S5 together suggest that the removal of Li induces the formation of very short S–S bonds and changes in the Fe–Fe distance.

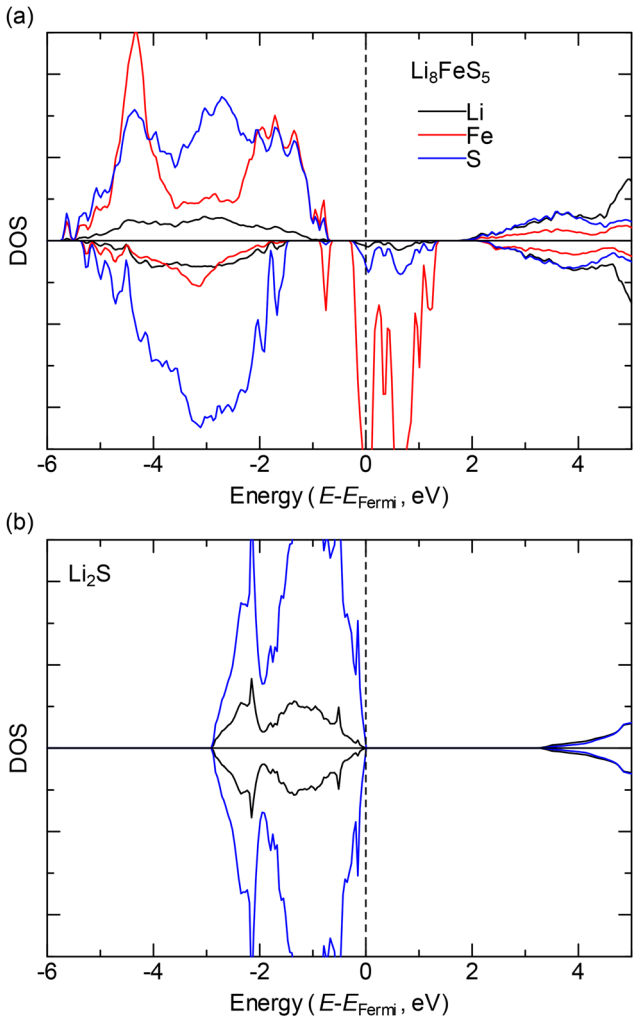

Fig. 9 Atom-decomposed DOS of (a) Li_8FeS_5 and (b) Li_2S.

4.2.5. Electronic DOS of Li_2S and Li_xFeS_5. The partial DOS of Li_2S and Li_8FeS_5 decomposed by elements are shown in Fig. 9. The majority and minority spin components are shown in the positive and negative directions along the vertical axis. There are slightly filled Fe 3*d* states immediately above the Fermi energy, which are absent in Li_2S, that facilitate electron conduction in Li_8FeS_5. The calculated DOS corroborates experimental results, in which the conductivity of Li_2S ($<10^{-10}$ S cm^{-1}) is much improved by introducing Fe (*ca.* 10^{-5} S cm^{-1} for Li_8FeS_5).

4.3. Insights on structural changes with cycling

The peaks in the EXAFS profiles shown in Fig. 4 are explained based on the calculated PDFs shown in Fig. 7 as follows. Although the EXAFS profiles in each sample are complicated and the peaks could not be assigned unambiguously, the main peak around 2.1 Å comes from the Fe–S bonds and additionally from the S–Li bonds in the S K-edge spectra. The *ca.* 4.0 Å S peak is the antifluorite structure NN peak. The 2.1 Å Fe peak barely changed during charging and discharging. In contrast, the *ca.* 4.0 Å S peak almost disappeared after charging and the *ca.* 2.3 Å S peak shifted to lower *r*. After discharge, the *ca.* 2 Å S peak position did not change and the *ca.* 4.0 Å S peak did not reappear when the charge voltage was 3.0 V, while the *ca.* 2 Å S peak position did revert and the *ca.* 4.0 Å S reappeared when the charge voltage was 2.6 V.

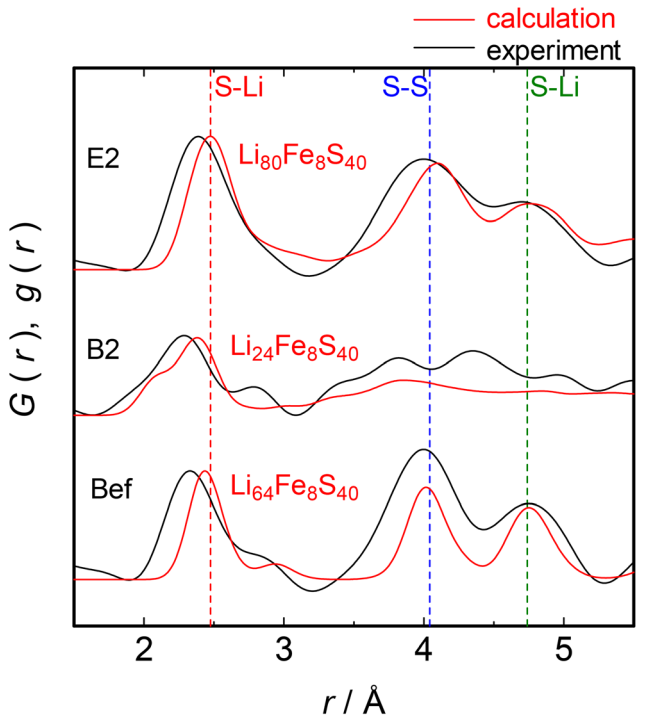

Fig. 10 Experimental RPDF *G*(*r*) and calculated PDF *G*(*r*). The experimental maximum charge voltage was 2.6 V. The sample labels of Bef, B2, and E2 correspond to positions in the charge and discharge process shown in Fig. 3(b).

Fig. 10 compares the experimental RPDFs before charging (Bef), after charging to 2.6 V (B2), and after full discharge (E2) with the calculated PDFs of Li_8FeS_5, Li_3FeS_5, and $Li_{10}FeS_5$. It is noteworthy that the computational Li_3FeS_5 model in Fig. 6(b) is significantly deformed from the Li_3FeS_5 model in Fig. 6(a), but still the PDF of Li_3FeS_5 shares features with the B2 RPDF (charge to 2.6 V). Some short-range ordering with S–S distances at *ca.* 4.0 Å, which is characteristic of the antifluorite structure, is found at this stage, suggesting that the fluorite structure may be recovered after Li insertion. Further charging that wipes out remnants of this short-range ordering causes a transformation into a completely different crystal structure.

5. Conclusions

We have investigated the decrease in the discharge capacity of Li_8FeS_5 when charged to 3.0 V *vs.* Li^+/Li, as compared to the case when charged to 2.6 V *vs.* Li^+/Li, by combining X-ray scattering and absorption methods with neural network potential calculations. In the framework of the antifluorite structure of Li_8FeS_5, S–S distances with *ca.* 4.0 Å cause disproportionation when Li is removed, and those around 2 Å, which are similar to what is found in S_8, gradually increase. Such disproportionation of S–S distances around 4.0 Å is rather restricted when charged to 2.6 V, while it does not when charged to 3.0 V. The *ca.* 4.0 Å S–S distances were therefore identified as a key indicator of the structural change reversibility in this antifluorite structure system.

Author contributions

Made substantial contributions to the conception and design of the study and performed computational simulation and interpretation: Takeuchi, T. and Hinuma, Y. Performed data acquisition for structural characterization: Ohara, K.; Kageyama, H.; Nakanishi, K.; Fujinami, S.; and Kiuchi, H. Supervised: Ohta, T. and Sakaebe, H. All authors revised the manuscript.

Conflicts of interest

There are no conflicts to declare.

Data availability

The data supporting this work are provided in the supplementary information (SI) or are available from the authors upon reasonable request.

Supplementary information is available. See DOI: https://doi.org/10.1039/d5dt02938d.

Acknowledgements

Part of this work was financially supported by the New Energy and Industrial Technology Development Organization (NEDO) under the RISING 2 project (JPNP16001). The synchrotron radiation experiments were performed at BL28XU in SPring-8 with the approval of the Japan Synchrotron Radiation Research Institute (JASRI) (Proposal No. 2019A7615, 2019B7615, and 2020A7615). The VESTA code[28] was used to draw Fig. 1, 6, and S5.

References

1 X. Ji and L. F. Nazar, *J. Mater. Chem.*, 2010, **20**, 9821–9826.
2 P. G. Bruce, S. A. Freunberger, L. J. Hardwick and J.-M. Tarascon, *Nat. Mater.*, 2012, **11**, 19–29.
3 P. Das and P. Sarkar, *Phys. Chem. Chem. Phys.*, 2023, **25**, 30536–30542.
4 M. N. Obrovac and J. R. Dahn, *Electrochem. Solid-State Lett.*, 2002, **5**, A70.
5 A. Hayashi, R. Ohtsubo, T. Ohtomo, F. Mizuno and M. Tatsumisago, *J. Power Sources*, 2008, **183**, 422–426.
6 T. Shigedomi, Y. Fujita, T. Kishi, K. Motohashi, H. Tsukasaki, H. Nakajima, S. Mori, M. Tatsumisago, A. Sakuda and A. Hayashi, *Chem. Mater.*, 2022, **34**, 9745–9752.
7 K. Han, J. Shen, C. M. Hayner, H. Ye, M. C. Kung and H. H. Kung, *J. Power Sources*, 2014, **251**, 331–337.
8 T. Takeuchi, H. Kageyama, K. Nakanishi, M. Ogawa, T. Ohta, A. Sakuda, H. Sakaebe, H. Kobayashi and Z. Ogumi, *J. Electrochem. Soc.*, 2015, **162**, A1745–A1750.
9 M. Nagao, A. Hayashi and M. Tatsumisago, *J. Mater. Chem.*, 2012, **22**, 10015–10020.
10 T. Takeuchi, H. Kageyama, K. Nakanishi, M. Tabuchi, H. Sakaebe, T. Ohta, H. Senoh, T. Sakai and K. Tatsumi, *J. Electrochem. Soc.*, 2010, **157**, A1196–A1201.
11 M. Otoyama, T. Takeuchi, N. Taguchi, K. Kuratani and H. Sakaebe, *ECS Adv.*, 2023, **2**, 010501.
12 T. Takeuchi, N. Taguchi, M. Kitta, T. Yaji, M. Otoyama, K. Kuratani and H. Sakaebe, *RSC Adv.*, 2024, **14**, 7229–7233.
13 T. Takeuchi, H. Kageyama, K. Nakanishi, H. Kiuchi, M. Katayama, Y. Inada, T. Ohta, T. Fukunaga, H. Sakaebe, H. Kobayashi and E. Matsubara, *J. Electrochem. Soc.*, 2019, **166**, A5231–A5236.
14 K. Shimoda, M. Murakami, T. Takeuchi, T. Matsunaga, Y. Ukyo, H. Sakaebe, H. Kobayashi and E. Matsubara, *J. Power Sources*, 2018, **398**, 67–74.
15 H. Tanida, K. Fukuda, H. Murayama, Y. Orikasa, H. Arai, Y. Uchimoto, E. Matsubara, T. Uruga, K. Takeshita, S. Takahashi, M. Sano, H. Aoyagi, A. Watanabe, N. Nariyama, H. Ohashi, H. Yumoto, T. Koyama, Y. Senba, T. Takeuchi, Y. Furukawa, T. Ohata, T. Matsushita, Y. Ishizawa, T. Kudo, H. Kimura, H. Yamazaki, T. Tanaka, T. Bizen, T. Seike, S. Goto, H. Ohno, M. Takata, H. Kitamura, T. Ishikawa, T. Ohta and Z. Ogumi, *J. Synchrotron Radiat.*, 2014, **21**, 268–272.
16 T. Proffen, S. J. L. Billinge, T. Egami and D. Louca, *Z. Kristallogr. - Cryst. Mater.*, 2003, **218**, 132–143.
17 S. Kohara, M. Itou, K. Suzuya, Y. Inamura, Y. Sakurai, Y. Ohishi and M. Takata, *J. Phys.: Condens. Matter*, 2007, **19**, 506101.
18 K. Ohara, Y. Kawakita, L. Pusztai, L. Temleitner, S. Kohara, N. Inoue and S. Takeda, *J. Phys.: Condens. Matter*, 2010, **22**, 404203.
19 A. Sakuda, K. Ohara, K. Fukuda, K. Nakanishi, T. Kawaguchi, H. Arai, Y. Uchimoto, T. Ohta, E. Matsubara, Z. Ogumi, T. Okumura, H. Kobayashi, H. Kageyama, M. Shikano, H. Sakaebe and T. Takeuchi, *J. Am. Chem. Soc.*, 2017, **139**, 8796–8799.
20 K. Nakanishi, S. Yagi and T. Ohta, *AIP Conf. Proc.*, 2010, **1234**, 931–934.
21 M. Kiguchi, T. Yokoyama, D. Matsumura, H. Kondoh, T. Ohta and Y. Kitajima, *Phys. Rev. B: Condens. Matter Mater. Phys.*, 1999, **60**, 16205–16210.
22 S. Takamoto, C. Shinagawa, D. Motoki, K. Nakago, W. Li, I. Kurata, T. Watanabe, Y. Yayama, H. Iriguchi, Y. Asano, T. Onodera, T. Ishii, T. Kudo, H. Ono, R. Sawada, R. Ishitani, M. Ong, T. Yamaguchi, T. Kataoka, A. Hayashi, N. Charoenphakdee and T. Ibuka, *Nat. Commun.*, 2022, **13**, 2991.
23 J. P. Perdew, K. Burke and M. Ernzerhof, *Phys. Rev. Lett.*, 1996, **77**, 3865–3868.
24 G. Kresse and J. Furthmüller, *Phys. Rev. B: Condens. Matter Mater. Phys.*, 1996, **54**, 11169–11186.
25 G. Kresse and D. Joubert, *Phys. Rev. B: Condens. Matter Mater. Phys.*, 1999, **59**, 1758–1775.
26 J. P. Perdew, A. Ruzsinszky, G. I. Csonka, O. A. Vydrov, G. E. Scuseria, L. A. Constantin, X. Zhou and K. Burke, *Phys. Rev. Lett.*, 2008, **100**, 136406.
27 Y. Hinuma, *Sci. Technol. Adv. Mater.:Methods*, 2024, **4**, 2409626.
28 K. Momma and F. Izumi, *J. Appl. Crystallogr.*, 2011, **44**, 1272–1276.